

## Electrochemistry

Experimental and Computational Studies of a Multi-Electron Donor–Acceptor Ligand Containing the Thiazolo[5,4-*d*]thiazole Core and its Incorporation into a Metal–Organic FrameworkFelix J. Rizzuto,<sup>[a]</sup> Thomas B. Faust,<sup>[a]</sup> Bun Chan,<sup>[a, b]</sup> Carol Hua,<sup>[a]</sup> Deanna M. D'Alessandro,<sup>\*[a]</sup> and Cameron J. Kepert<sup>\*[a]</sup>

**Abstract:** A ligand containing the thiazolo[5,4-*d*]thiazole (TzTz) core (acceptor) with terminal triarylamine moieties (donors), *N,N'*-(thiazolo[5,4-*d*]thiazole-2,5-diylbis(4,1-phenylene))bis(*N*-(pyridine-4-yl)pyridin-4-amine) (**1**), was designed as a donor–acceptor system for incorporation into electronically active metal–organic frameworks (MOFs). The capacity for the ligand to undergo multiple sequential oxidation and reduction processes was examined using UV/Vis-near-infrared spectroelectrochemistry (UV/Vis-NIR SEC) in combination with DFT calculations. The delocalized nature of the highest occupied molecular orbital (HOMO) was found to inhibit charge-transfer interactions between the terminal triaryla-

mine moieties upon oxidation, whereas radical species localized on the TzTz core were formed upon reduction. Conversion of **1** to diamagnetic 2+ and 4+ species resulted in marked changes in the emission spectra. Incorporation of this highly delocalized multi-electron donor–acceptor ligand into a new two-dimensional MOF, [Zn(NO<sub>3</sub>)<sub>2</sub>(**1**)] (**2**), resulted in an inhibition of the oxidation processes, but retention of the reduction capability of **1**. Changes in the electrochemistry of **1** upon integration into **2** are broadly consistent with the geometric and electronic constraints enforced by ligation.

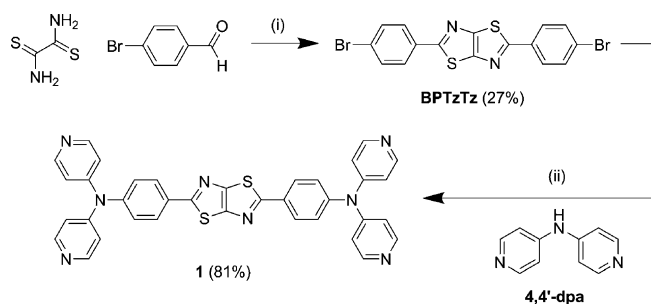
## Introduction

Metal–organic frameworks (MOFs)<sup>[1]</sup> are a versatile class of materials capable of displaying a plethora of tunable properties.<sup>[2]</sup> Though early research in the field was motivated by the potential applications of MOFs in molecular storage, catalytic conversion, and chemical separation,<sup>[3]</sup> focus has shifted in recent years towards the creation of multifunctional materials that are capable of responding to external stimuli. A particular challenge has been the realization of conductivity,<sup>[4]</sup> magnetism,<sup>[5]</sup> and shape memory,<sup>[6]</sup> properties that underpin potential technological applications in battery materials and molecular electronics devices, to name a few.

The design and synthesis of charge-transfer MOFs containing donor and acceptor functionalities represents an important step towards the goal of realizing electronically conductive multidimensional materials.<sup>[4a]</sup> With the ability to be both re-

duced and oxidized, these systems enable insights into electron transfer phenomena in three-dimensional coordination space. To date, however, focus has largely been placed on monitoring electron transfer and charge mobility between the ligand components of these materials, rather than within the ligands themselves.<sup>[7]</sup> Whereas the former approach often relies on strong  $\pi$ -stacking between proximal redox-active units (i.e., by interligand charge transfer) to facilitate long-range interactions, an intraligand approach has the potential to create MOFs that exhibit short-range, localized charge transfer.

Here, we report a new donor–acceptor–donor (DAD) ligand (**1**) incorporating the thiazolo[5,4-*d*]thiazole (TzTz) core (acceptor) functionalized with terminal triarylamine moieties (donors), shown in Scheme 1. Electrochemical, UV/Vis-NIR solution state



**Scheme 1.** Synthesis of ligand **1**. Reagents and conditions: (i) DMF, reflux, 3 h. (ii) CuSO<sub>4</sub>, 18-crown-6, K<sub>2</sub>CO<sub>3</sub>, diphenyl ether, 200 °C, 6 days.

[a] F. J. Rizzuto, Dr. T. B. Faust, Dr. B. Chan, C. Hua, Dr. D. M. D'Alessandro, Prof. C. J. Kepert  
School of Chemistry  
The University of Sydney, NSW 2006 (Australia)  
Fax: (+61) 29351 3329  
E-mail: deanna.dalessandro@sydney.edu.au  
cameron.kepert@sydney.edu.au

[b] Dr. B. Chan  
ARC Centre of Excellence for Radical Chemistry and Biotechnology  
The University of Sydney, NSW 2006 (Australia)

Supporting information for this article is available on the WWW under <http://dx.doi.org/10.1002/chem.201405089>.

spectroelectrochemical, and DFT calculations are employed to elucidate the electronic properties of this ligand. The incorporation of **1** into a two-dimensional framework,  $[\text{Zn}(\text{NO}_3)_2(\mathbf{1})]$  (**2**), has revealed important, fundamental insights into the influence of donor–acceptor–donor ligands on the electronic properties of metal-organic frameworks.

The TzTz functionality has received limited attention as a component of inorganic systems; however, it has been incorporated into a number of purely organic polymers to yield materials with easily accessible reduced states. The electrochemical nature of the TzTz moiety has only been explored sparingly in discrete molecules<sup>[8]</sup> and polymeric systems,<sup>[9]</sup> and the accessibility, relative energies, and orbital contributions of its redox states have not been fully elucidated.<sup>[10]</sup> Instead, focus has largely been placed on the incorporation of TzTz into charge transfer systems by coupling the electron accepting (*n*-type) behavior of the moiety with that of an electron donor (*p*-type), creating extended organic compounds displaying sought-after electrical properties.<sup>[11]</sup> Though initially focused on biological activity, the discovery of the photophysical properties of TzTz in organic systems has led to the creation of semiconducting polymers,<sup>[12]</sup> field-effect transistors<sup>[8a]</sup> and optical devices.<sup>[8b]</sup>

The bis(triarylamine) functionality, by virtue of its well-known ability to generate mixed-valence states upon chemical and electrochemical oxidation, was selected as the donor moiety in the present work. In mixed-valence systems where the triarylamine centers are bridged by conjugated diamagnetic substituents, intervalence charge transfer (IVCT) can arise as a result of electron transfer between the units in different formal oxidation states.<sup>[13]</sup> In turn, this facilitates magnetic interactions,<sup>[14]</sup> electrical conductivity,<sup>[15]</sup> and fluorescence,<sup>[16]</sup> which have previously been studied in discrete bis(triarylamine) molecules.

The incorporation of redox-active or paramagnetic components between charge-transferring triarylamine centers has not been investigated as a strategy for designing charge-transfer MOFs, and has seldom been investigated even in small-molecule systems. By contrast, the triarylamine moiety has been incorporated into a range of purely organic systems to generate semiconductivity; however, the electronic properties of these materials, and the mechanisms of charge transfer in the solid state, have not been investigated. As a result, the present work seeks to elucidate the electronic properties of ligand **1** as a potential candidate for the construction of multidimensional assemblies that exhibit fundamentally interesting and technologically relevant charge-transfer phenomena.

## Results and Discussion

### Synthesis and electronic properties of **1**

The synthesis of **1** (Scheme 1) involved the initial preparation of dibromophenyl-thiazolo[5,4-*d*]thiazole (BPTzTz) from the condensation of 4-carboxybenzaldehyde and dithiooxamide. Coupling this intermediate with excess 4,4'-dipyridylamine (4,4'-dpa) in a Goldberg reaction afforded **1** in good yield (81%). Stoichiometric quantities of copper sulfate and high

temperatures (200 °C) were required for the reaction to proceed. When lower temperatures were used, a significant decrease in the yield was observed for the disubstituted product (36%), and the monosubstituted adduct was isolated as the major product (47%).

Solution state cyclic voltammetry (CV) was conducted on **1** in  $[\text{nBu}_4\text{N}]\text{PF}_6/\text{MeCN}$  electrolyte (0.1 M) with scan rates in the range 50–200  $\text{mV s}^{-1}$  (see Figure 1). At 100  $\text{mV s}^{-1}$ , three pro-

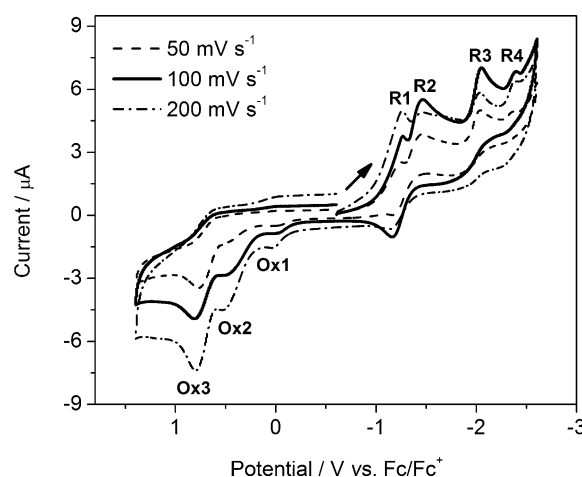


**Figure 1.** CV of **1** in  $[\text{nBu}_4\text{N}]\text{PF}_6/\text{MeCN}$  electrolyte (0.1 M) over scan rates in the range 50–200  $\text{mV s}^{-1}$ . The arrow indicates the direction of the forward scan.

cesses were observed at 0.035, 0.52 and 0.81 V versus  $\text{Fc}/\text{Fc}^+$  in the anodic region, whereas four processes were observed at  $-1.24$ ,  $-1.45$ ,  $-2.04$  and  $-2.37$  V versus  $\text{Fc}/\text{Fc}^+$  in the cathodic region. A plot of the current against the square root of the scan rate according to the Randles–Sevcik equation indicated that all three oxidation processes and the first reduction process were reversible, whereas the final three reduction processes were quasi-reversible (Figure S1 in the Supporting Information).

### Oxidation properties of **1**

Solution state UV/Vis-NIR SEC was conducted on **1** to deduce the extent of the interaction between the donor and acceptor moieties, and to elucidate the presence, if any, of charge-transfer interactions between triarylamine centers. In general, the appearance of stable isosbestic points for each process indicated that no chemical decomposition occurred, and that the spectra corresponded to individual redox processes, as identified by CV (Figure 1). As shown in Figure 2 (shown fully in Figure S2 in the Supporting Information), three oxidative processes were identified (Ox1–3), corresponding to the three redox waves observed in the anodic region in Figure 1. The first process (Ox1) is characterized by an increase in the shoulder peak at  $33200\text{ cm}^{-1}$  and a decrease in the bands at  $34050$  and  $25600\text{ cm}^{-1}$ , the latter of which undergoes a blueshift to  $25880\text{ cm}^{-1}$ . In contrast, the second process (Ox2) results in a decrease in the UV peak and the formation of a new band at

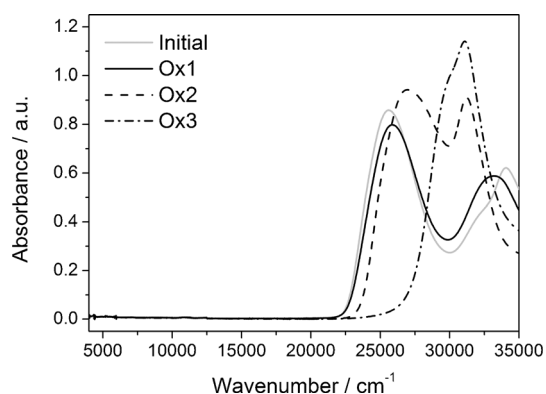


**Figure 2.** Summary of the oxidation processes captured in the SEC of **1** in  $[n\text{Bu}_4\text{N}]\text{PF}_6/\text{MeCN}$  electrolyte (0.1 M).

lower energy ( $31\,220\text{ cm}^{-1}$ ), as well as an increased intensity and blueshift in the band at  $25\,880$  to  $26\,920\text{ cm}^{-1}$ . The third process (Ox3) is characterized by an intensification of the  $31\,220\text{ cm}^{-1}$  band and the appearance of a shoulder peak at approximately  $30\,000\text{ cm}^{-1}$ , and also a decrease of the peak at  $26\,920\text{ cm}^{-1}$ . Of particular note is the absence of characteristic triarylamine-based radical or IVCT bands in the visible or NIR regions in any process.

Given the small spectral changes and low current associated with Ox1, no major structural or redox changes are envisioned. DFT calculations suggest that free rotation around the phenylamine bonds enables a change in the optimal geometry upon application of a low potential, suggesting that the neutral ligand may convert to a partially charged species with an altered geometry prior to formal redox processes. Given that a current (albeit weak) is observed for Ox1, electronic changes must be occurring within the ligand regardless. As both the FTIR spectrum and elemental analysis indicate the presence of  $\text{H}_2\text{O}$  in the crystal lattice of **1**, we postulate that oxidation of the pyridyl substituents to their respective pyridyl-N oxide species occurs during Ox1, leading to only minor spectral shifts during SEC.

The spectral progressions corresponding to Ox2 and Ox3 were likewise investigated by DFT calculations, and specifically by the distribution of electron density in the HOMO-1 to LUMO of **1** (Figure 3). Importantly, the coplanarity of the TzTz and phenyl functionalities leads to a flat bridge between the amine centers, resulting in a HOMO that is delocalized over the ligand backbone. In contrast, the electron density in the HOMO-1 is localized around the tertiary amine centers. Removing electrons from the ligand in its ground state therefore removes electron density from the entire molecule, and not just the triarylamine centers. As a result, upon oxidation, **1** does not undergo radical formation (as reflected by the lack of low-energy bands forming during SEC). Instead, di- and tetracation states form upon two sequential  $2e^-$  oxidation processes. During Ox2, two electrons are removed from the HOMO, and a further two electrons are removed from the triarylamine centers (i.e., the HOMO-1 during Ox3).

The absence of characteristic triarylamine-based radical bands is thus ascribed to the simultaneous oxidation of the

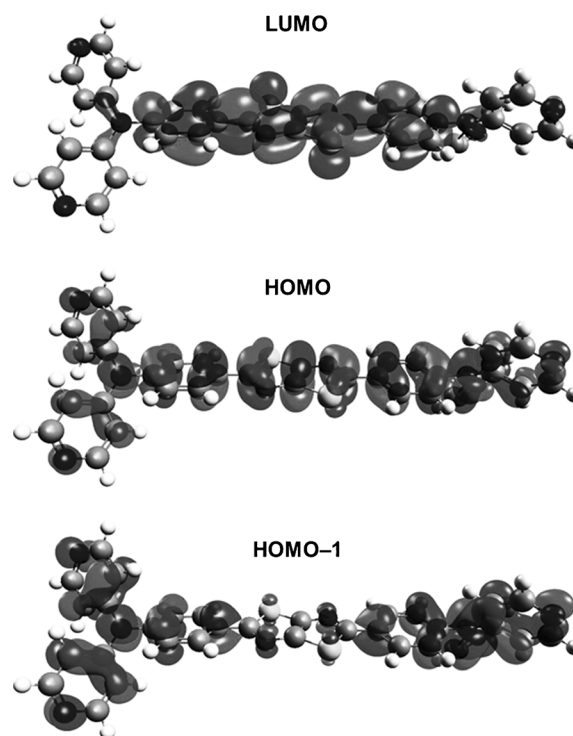


**Figure 3.** Molecular orbitals of **1** obtained from DFT calculations.

two triarylamine functionalities to their singly- then doubly-oxidized states. Rather than viewing the donor and acceptor components separately, the ligand must be viewed as a delocalized entity owing to the high degree of coplanarity between the triarylamine centers. In cases where triarylamines are bridged by lengthy, flexible organic units, the redox-active centers can be oxidized in isolation, facilitating radical formation and IVCT.<sup>[13]</sup>

### Reduction properties of **1**

Four processes were observed during the reductive SEC of **1** (Figure 4 and Figure S3 in the Supporting Information) corresponding to the four redox waves observed in the cathodic region of the CV shown in Figure 1. Small spectral changes observed in the first reduction process (R1) are likely to arise from slight geometrical changes and the interaction of the pyridyl units with lattice  $\text{H}_2\text{O}$ . During the second process (R2) a weak band appears at approximately  $19\,300\text{ cm}^{-1}$  and is accompanied by the appearance of a peak at  $26\,670\text{ cm}^{-1}$ , the re-appearance and intensification of the shoulder band at  $33\,220\text{ cm}^{-1}$ , and the disappearance of the UV peak at  $33\,940\text{ cm}^{-1}$  (Figure S3 in the Supporting Information). In the third process (R3), prominent bands appear in the region  $12\,500$ – $22\,500\text{ cm}^{-1}$  and the  $\pi \rightarrow \pi^*$  transition at  $25\,330\text{ cm}^{-1}$  disappears, as shown in Figure 4. Though the newly formed band at  $26\,670\text{ cm}^{-1}$  likewise decreases, the UV band at  $33\,940\text{ cm}^{-1}$  increases. The fourth process (R4) does not appear to accompany any significant electronic shift, other than minor intensity changes in the low-energy radical bands (Figure S3 in the Supporting Information).

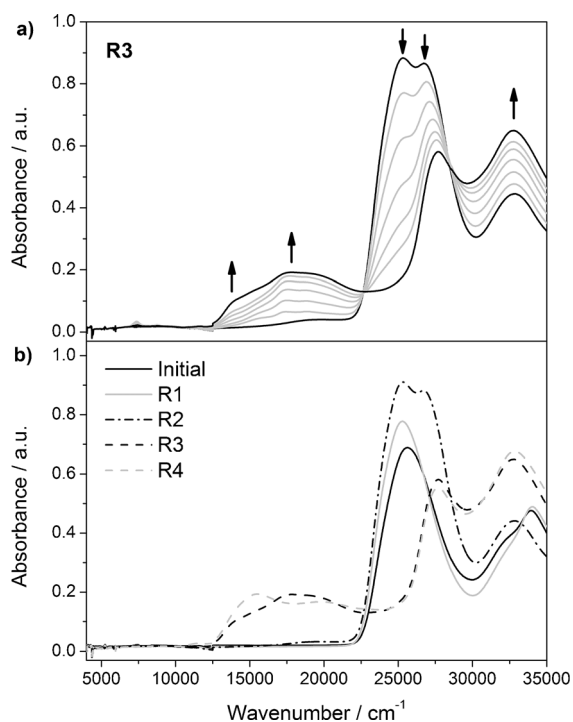


**Figure 4.** a) The third process (R3) captured in the reductive SEC of **1** in  $[n\text{Bu}_4\text{N}]\text{PF}_6/\text{MeCN}$  electrolyte (0.1 M), and b) a summary of the reduction processes captured in the SEC of **1**. The arrows in a) show the direction of change in the spectrum during R3.

The formation of a radical species during R3 was implied by the appearance of low-energy bands in the region 12500–22500  $\text{cm}^{-1}$  (Figure 4) and further confirmed by EPR spectroscopy. Ex situ reduction of **1** with lithium naphthalenide (LiNp) in THF resulted in a spectrum with  $g=2.0025$  (Figure S4 in the Supporting Information). According to the geometries of the LUMO (Figure 3) and LUMO + 1 (Figure S5 in the Supporting Information) orbitals, electron additions are localized on the TzTz center, as expected from the electron-accepting nature of the moiety. Whereas initial oxidations occur from delocalized orbitals, reductions occur in localized ones.

Though regeneration of the starting spectrum was observed for the reductive SEC, applying a potential of 0 V after reaching Ox3 in the oxidative SEC of **1** resulted in a spectrum correlating to Ox1, as opposed to that of the neutral ligand (Figure S2 in the Supporting Information). The integrity of the ligand was verified by collecting the  $^1\text{H}$  NMR spectra of **1** after the electrical generation of its fully reduced and oxidized species. The similarity of the proton spectra to the neutral species indicated that the ligand remained intact during all redox processes.

The formal reduction and oxidation processes are summarized in Table 1. The degree of rotation of the dipyridylamine moieties upon both reduction and oxidation is also detailed in Table 1, indicating that slight torsion of the terminal moieties may occur prior to, or concurrent with, each of the formal redox processes.

	Process	Charge	Angle [°]
	Ox3	4+	24
	Ox2	2+	20
	R3	0	45
	R4	1–	62
	R4	2–	62

### Fluorescence properties of oxidized **1**

UV/Vis bands for the neutral ligand at 25610 and 34060  $\text{cm}^{-1}$  (and the shoulder peak at ca. 31800  $\text{cm}^{-1}$ ) are all assigned to  $\pi \rightarrow \pi^*$  transitions. Upon excitation of the yellow solution at 25610  $\text{cm}^{-1}$ , a redshifted fluorescence band was observed at 21370  $\text{cm}^{-1}$ , resulting in a blue emission. Given that the HOMO is delocalized over the molecule while the LUMO is localized on the central bridge between triarylamine centers, electron excitation at 25610  $\text{cm}^{-1}$  is localized predominantly on the TzTz center.

Stoichiometric additions of  $\text{NOPF}_6/\text{MeCN}$  solution (a  $1e^-$  oxidant; 0.87 vs.  $\text{Fc}/\text{Fc}^{+}$ )<sup>[17]</sup> to a solution of **1** in MeCN resulted in a change in the fluorescence of the ligand. The addition of a  $1e^-$  portion of the oxidizing agent resulted in a slight decrease in the fluorescence intensity at 21370  $\text{cm}^{-1}$ , further indicating that no formal redox process was occurring during Ox1 (Figure S6 in the Supporting Information). Upon a  $2e^-$  oxidation, the maximum of the emission spectrum instead occurred at 23200  $\text{cm}^{-1}$ , whereas the use of excess oxidant resulted in a fluorescence maximum at 19800  $\text{cm}^{-1}$ ; the ligand fluoresces light blue in its neutral state, royal blue in its 2+ oxidation state, and green in its 4+ oxidation state. The Stokes shifts were measured to be 4200, 4180, and 7620  $\text{cm}^{-1}$ , respectively, for each state. Importantly, the fluorescence was not quenched by the addition of oxidant. Given the distinct transitions associated with the different oxidation states of **1**, the material shows promise as a potential chemosensor, particularly for the detection of chemical oxidants.

UV/Vis absorbance and emission spectra of **1** oxidized with stoichiometric portions of  $\text{NOPF}_6/\text{MeCN}$  are shown in Figure 5. With the exception of  $1^{4+}$ , the UV/Vis spectra correlate well to the processes identified by oxidative SEC (Figure 2). The deviation of approximately 33 nm between the electrically and chemically generated 4+ species is attributed to the different experimental conditions, as well as the different counterions (and the concentration of these counterions) present in the respective solutions, leading to different solvent reorganization and ion-pairing energies.

### Incorporation of **1** into a metal–organic framework

Single crystals of  $[\text{Zn}(\text{NO}_3)(\mathbf{1})]$  (**2**) suitable for X-ray diffraction studies were synthesized by slowly cooling a 1:1 MeCN:DMF solution containing **1** and  $\text{Zn}(\text{NO}_3)_2 \cdot x\text{H}_2\text{O}$  that had been heated to 120 °C. The structure (shown in Figure 6) consists of octahe-

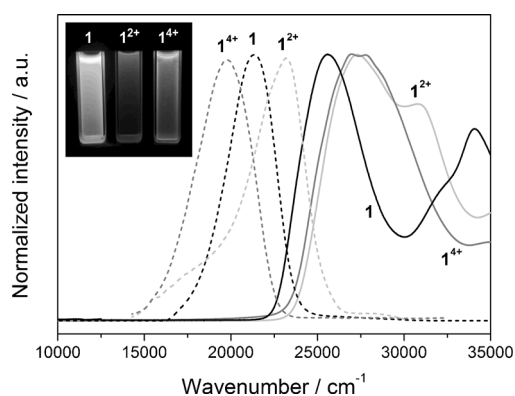


**Figure 5.** UV/Vis absorbance (bold lines) and fluorescence emission (dashed lines) spectra of **1** in different formal oxidation states, and the coloration obtained upon excitation with a UV lamp at  $27400\text{ cm}^{-1}$  ( $365\text{ nm}$ ) (inset).

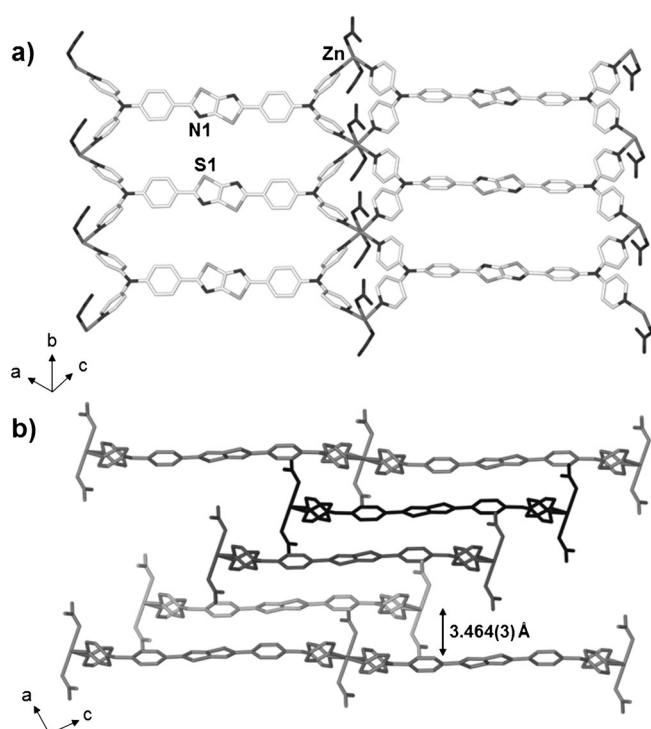


**Figure 6.** Crystal structure of **2**. a) A single 2D sheet of **2**, and b) crystal packing of 2D sheets viewed along the *b*-axis. Hydrogen atoms and nitrate disorder are omitted for clarity.

dral  $\text{Zn}^{\text{II}}$  centers connected equatorially to four pyridyl moieties (of four separate ligands) and axially to two nitrate anions, which are partially disordered. The resulting two-dimensional sheets stack such that the ligand phenyl rings overlap the TzTz centers of the layers above and below, creating a series of symmetry-generated layers separated by a distance of  $3.464(3)\text{ \AA}$ . Because the phenyl rings are almost coplanar with the TzTz unit (torsion angle =  $9^\circ$ ), the pyridyl groups adopt a propeller-like conformation, commensurate with structurally analogous triarylamine functionalities.<sup>[18]</sup> An intramolecular distance of  $15.784(4)\text{ \AA}$  separates the triarylamine centers. The pore dimension viewed along the *a*-axis measures  $4.2\text{ \AA}$  (be-

tween opposing S1 and N1) by  $11.3\text{ \AA}$  (between Zn centers), giving the framework one-dimensional, solvent-accessible channels.

### Electronic properties of **2**: the effect of structural rigidity

Though the solution state CV of **1** indicated that the ligand undergoes three oxidation processes, solid state CV conducted on **2** (Figure S7 in the Supporting Information) revealed that no oxidation processes occur in the framework. To confirm this, oxidative solid-state SEC conducted on **2** in  $[\text{nBu}_4\text{N}]\text{PF}_6/\text{MeCN}$  electrolyte did not reveal any significant spectral change over applied potentials in the range  $0\text{--}2.5\text{ V}$  (Figure S8 in the Supporting Information), indicating that no significant electronic or redox change was occurring.

Similarities between the reductive electrochemistry of **1** and **2** are evident. The two cathodic processes observed at  $-2.12$  and  $-2.44\text{ V}$  versus  $\text{Fc}/\text{Fc}^+$  in the CV of **2** were also followed using solid-state SEC.<sup>[19]</sup> The appearance of lower-energy bands at  $15800$  and  $18800\text{ cm}^{-1}$  in the second process (Figure 7) in-

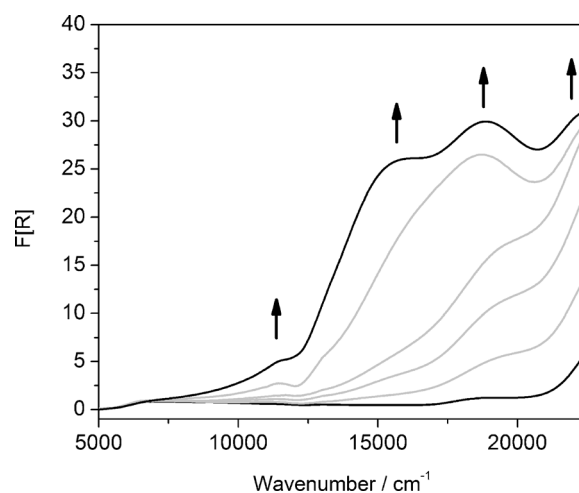


**Figure 7.** The second reduction process captured in the solid state SEC of **2** in  $[\text{nBu}_4\text{N}]\text{PF}_6/\text{MeCN}$  electrolyte ( $0.1\text{ M}$ ), held at  $-2.5\text{ V}$ . The arrows show the direction of change in the spectrum.

icates the formation of a radical species. Unlike the SEC of the free ligand, however, the intermediate process (R2 in the SEC of **1**) does not occur. This may be due to the rigidity of the ligand, which is enforced in the solid state: ligation would prevent the increase in torsion that occurs between TzTz and triarylamine moieties during the solution state reduction of **1**, thereby altering the number of processes observed. A similar hypothesis may also be applied to explain the absence of oxidation processes observed in **2**, such that electron removal is inhibited by the decreased rotation permitted by the ligands in the framework.

The difference in redox behavior between the free and bound ligand was studied further by exposing **1** and **2** to  $\text{I}_2$ . Spectra of **1** oxidized with portions of  $\text{I}_2$  in MeCN indicated conversion to at least Ox2 (Figure S11 in the Supporting Infor-

mation), and complete conversion to Ox3 was verified by fluorescence; however, the difficulties associated with spectral assignment in the solid state necessitated a different approach for the analysis of the framework. Thus, the redox properties of **2** were further explored by exposing the material to I<sub>2</sub> vapor and conducting a crystallographic analysis. This was achieved by coating a single crystal of **2** in paratone-*N* oil and suspending it on the inner wall of a small glass vial containing a few grains of solid iodine, allowing I<sub>2</sub> to diffuse throughout the chamber and penetrate the pores of the framework at a slow and controlled rate. The initial yellow crystal turned dark red over three days, suggesting iodine intercalation. The resultant structure, **2**·I<sub>2</sub>, was characterized by single crystal X-ray diffraction to ascertain the effects of intercalation on the framework. A structural comparison of the neutral and doped frameworks is provided in Figure 8, and is accompanied by photographs of the crystal upon I<sub>2</sub> exposure.

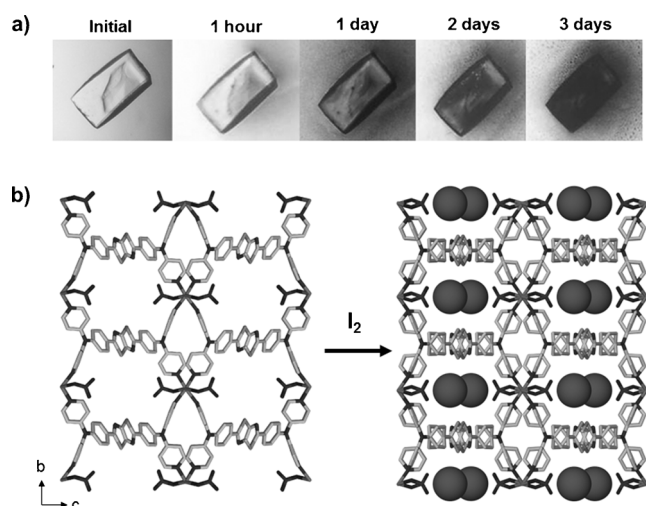


**Figure 8.** a) Images of a crystal of **2** upon exposure to I<sub>2</sub> at various times, and b) a comparison of neutral **2** and **2**·I<sub>2</sub> viewed down the *a*-axis. Hydrogen atoms are omitted for clarity.

Considerable changes in the structure were observed upon exposure to I<sub>2</sub>. In addition to the incorporation of I<sub>2</sub> into the pores, which refined as a statistically disordered I<sub>2</sub> molecule with 26% occupancy, there are clear changes to the framework structure, the most pronounced being the disordering of the TzTz units, whereas previously these had adopted an undulating configuration along the *c*-axis (see Figure 8b). This order-disorder transformation involves the introduction of mirror symmetry perpendicular to *b*, with an associated approximate halving of the *c*-axis (from 26.668(2) Å to 13.636(2) Å) and a change in space group from *P2<sub>1</sub>/n* to *P2<sub>1</sub>m*.

Though the considerable changes observed crystallographically indicate that structural variations occur upon iodine exposure, both with regards to crystal symmetry and disorder, the ligand does not appear to undergo oxidation changes in the solid state. This is evidenced by the relatively similar bond lengths in **2** and **2**·I<sub>2</sub> (although the degree of disorder in the iodized framework makes this comparison somewhat ambigu-

ous) and by the assignment of I<sub>2</sub> rather than associated anionic species within the pores. This observation is consistent with the CV results for **2**.

## Conclusion

The new redox-active DAD ligand **1** was designed to exhibit charge transfer properties of interest for incorporation into electronically active metal-organic frameworks. CV and SEC measurements conducted on the organic ligand indicated a series of complex electrochemical processes that were clarified using DFT calculations and EPR spectroscopy. The ligand sequentially loses two electrons upon oxidation to form a diamagnetic species in the 2+ and 4+ oxidation states, whereas reduction causes radical formation. No IVCT interactions between triarylamine redox centers were evident in either case. Rather than acting separately as donor and acceptor components, the triarylamine and TzTz functionalities in the ligand act as a single delocalized unit, as reflected in the DFT calculations for the HOMO of the ground state. The geometry of the ligand, as well as the incorporation of the electron-accepting TzTz redox-active moiety, inhibits IVCT between triarylamine centers within **1**. Thus, the coplanarity between triarylamine moieties, and the resulting delocalization of the HOMO, prevents the terminal functionalities from undergoing localized oxidation processes.

Though the presence of radicals often quenches fluorescence, the sequential oxidation states of **1** exhibited different fluorescence maxima, further confirming the presence of diamagnetic species throughout oxidation. The ligand emits a light blue, royal blue, and green color upon oxidation from the neutral, to 2+ and 4+ redox states, respectively.

Upon the inclusion of **1** into a metal-organic framework, **2**, the electronic properties of the ligand were markedly altered. Though the ligand still underwent radical formation during reduction, no oxidation processes were observed. Intercalation of I<sub>2</sub> in the solid state resulted in significant disorder and a change in crystal packing, but oxidation of the organic unit did not occur. By comparing the electrochemical nature of the free and bound ligand, we have demonstrated that the electronic properties of redox-active ligands can be inhibited upon inclusion into MOFs, and that the functional properties of multidimensional materials are not necessarily represented by those of their components.

## Experimental Section

All reagents and solvents employed were commercially available and used as received without further purification. For electrochemical experiments, MeCN was dried over CaH<sub>2</sub> and distilled under N<sub>2</sub>, while tetrabutylammonium hexafluorophosphate ([*n*Bu<sub>4</sub>N]PF<sub>6</sub>) was recrystallized three times from absolute EtOH before being dried in vacuo. 4,4'-Dipyridylamine (4,4'-dpa) was synthesized by following a literature procedure.<sup>[20]</sup>

## 2,5-Bis(4-bromophenyl)thiazolo[5,4-*d*]thiazole (BPTzTz)

The compound was synthesized using a modification of literature procedures.<sup>[21]</sup> A solution of dithiooxamide (1.2 g, 10 mmol) and 4-bromobenzaldehyde (4.0 g, 22 mmol) in DMF (40 mL) was refluxed for 3 h. The mixture was filtered, washed with water, and the residue recrystallized from cyclohexanone to afford BPTzTz as a yellow solid (1.2 g, 27%, m.p. > 260 °C); <sup>1</sup>H NMR (300 MHz, *d*<sub>5</sub>-pyridine): δ = 7.98 (d, *J* = 8.7 Hz, 4H), 7.69 ppm (d, *J* = 8.6 Hz, 4H); <sup>13</sup>C NMR (75 MHz, *d*<sub>5</sub>-pyridine): δ = 176.7, 141.5, 140.7, 132.5, 128.1, 125.1 ppm; IR (KBr):  $\tilde{\nu}$  = 1442, 1068, 1004, 840, 811 cm<sup>-1</sup>; LR-APCI-MS *m/z* 453 [M]<sup>+</sup>. HR-APCI-MS *m/z* calcd for C<sub>16</sub>H<sub>8</sub>Br<sub>2</sub>N<sub>2</sub>S<sub>2</sub>: 452.85534 [M]<sup>+</sup>; found: 452.76054; elemental analysis calcd (%) for C<sub>16</sub>H<sub>8</sub>Br<sub>2</sub>N<sub>2</sub>S<sub>2</sub>: C 42.50, H 1.78, N 6.20; found: C 41.92, H, 1.90; N, 6.15.

## *N,N'*-(Thiazolo[5,4-*d*]thiazole-2,5-diylbis(4,1-phenylene))-bis(*N*-(pyridine-4-yl)pyridin-4-amine (1)

4,4'-Dpa (430 mg, 2.5 mmol), BPTzTz (450 mg, 1.0 mmol), anhydrous potassium carbonate (690 mg, 5.0 mmol), anhydrous copper sulfate (150 mg, 0.90 mmol), 18-crown-6 (36 mg, 0.15 mmol), and diphenyl ether (10 mL) were heated at 200 °C for 6 days. After the reaction had cooled, water (20 mL) was added. The aqueous layer was extracted with CH<sub>2</sub>Cl<sub>2</sub> (3 × 100 mL), and the organic layer dried over NaSO<sub>4</sub>. The solvent was removed under reduced pressure and the residue purified by silica gel column chromatography (using an elution gradient of 20:1 CH<sub>2</sub>Cl<sub>2</sub>:Et<sub>3</sub>N to 20:1:1 CH<sub>2</sub>Cl<sub>2</sub>:Et<sub>3</sub>N:MeOH) to afford the title compound as a dark yellow solid (510 mg, 81%, m.p. > 260 °C); <sup>1</sup>H NMR (300 MHz, [D<sub>6</sub>]DMSO): δ = 8.46 (dd, *J* = 4.8, 1.5 Hz, 8H), 8.12 (dd, *J* = 6.7, 2.0 Hz, 4H), 7.37 (dd, *J* = 6.7, 2.0 Hz, 4H), 7.06 ppm (dd, *J* = 4.8, 1.5 Hz, 8H); <sup>13</sup>C NMR (75 MHz, [D<sub>6</sub>]DMSO): δ = 167.7, 151.3, 151.0, 150.5, 146.2, 130.6, 128.1, 127.2, 117.0 ppm; IR (KBr):  $\tilde{\nu}$  = 3038, 1577, 1494, 1339, 1287, 1217, 818, 735, 625, 535 cm<sup>-1</sup>; LR-ESI-MS *m/z* 633 [M]<sup>+</sup>. HR-ESI-MS *m/z* calcd for C<sub>36</sub>H<sub>25</sub>N<sub>8</sub>S<sub>2</sub>: 633.15989 [M]<sup>+</sup>; found: 633.16412; elemental analysis calcd (%) for C<sub>36</sub>H<sub>24</sub>N<sub>8</sub>S<sub>2</sub>·4H<sub>2</sub>O: C 61.15, H 4.32, N 15.75; found: C 61.36, H, 4.57; N, 15.90.

## [Zn(NO<sub>3</sub>)<sub>2</sub>](1) (2)

Single crystals were grown by heating Zn(NO<sub>3</sub>)<sub>2</sub>·6H<sub>2</sub>O (10 mg, 0.03 mmol) and **1** (1 mg, 2 μmol) in a 1:1 MeCN:DMF solution (5 mL) at 120 °C for 72 h, followed by cooling to room temperature over 12 h. Heating **1** (40 mg, 0.063 mmol) and Zn(NO<sub>3</sub>)<sub>2</sub>·6H<sub>2</sub>O (40 mg, 0.15 mmol) in the same solvent system (15 mL) at 120 °C for 48 h with stirring yielded a yellow powder of **2** (34 mg, 66%).

**Oxidation of the ligand by NOPF<sub>6</sub>**: **1** was dissolved in dry MeCN (6 mL) and oxidized using a stoichiometric amount (1, 2, and 4e<sup>-</sup> equivalents) of 5 × 10<sup>-3</sup> M NOPF<sub>6</sub>/MeCN solution, through which N<sub>2</sub> was bubbled for 10 min, facilitating the removal of NO.

**Reduction of the ligand by LiNp**: **1** was suspended in THF (2 mL) and reduced with a 4e<sup>-</sup> equivalent of LiNp/THF solution (0.1 M). H<sub>2</sub>O (1 mL) was subsequently added to oxidize any remaining naphthalenide radical and the solution was stirred under Ar for one hour.

**Impregnation of the framework by I<sub>2</sub>**: A small 2 mL glass vial containing the neutral crystal coated in paratone-*N* oil was placed inside a larger 21 mL glass vial containing solid iodine, which was allowed to diffuse throughout the chamber.

## Single-crystal X-ray diffraction

Diffraction data for **2** were collected on a Bruker-Nonius FR951 Kappa APEX II equipped with a MoK $\alpha$  ( $\lambda$  = 0.71073 Å) radiation source. For **2·I<sub>2</sub>**, data were collected on an Agilent Technologies SuperNova diffractometer, employing CuK $\alpha$  ( $\lambda$  = 1.5406 Å) radiation. An Oxford Cryosystems 700 Plus cryostream attachment produced a continuous stream of N<sub>2</sub> at 150 K in both cases. Following harvest, crystals were coated in a thin film of paratone-*N* oil and mounted on a mohair fiber affixed to a goniometer head. Data reduction, integration and absorption corrections were performed using the Agilent Technologies CrysAlisPro<sup>[22]</sup> software (version 1.171.35.8) for the SuperNova collection, while the APEX II collection was processed using SAINT+<sup>[23]</sup> within the APEX2 software suite. Crystal structures were solved using SUPERFLIP<sup>[24]</sup> and refined within SHELXL-97<sup>[25]</sup> using the full-matrix least-squares on *F*<sup>2</sup> method.

CCDC-1012472(**2**) and CCDC-1012473(**2·I<sub>2</sub>**) contain the supplementary crystallographic data for this paper. These data can be obtained free of charge from The Cambridge Crystallographic Data Centre via www.ccdc.cam.ac.uk/data\_request/cif.

Crystal data for C<sub>36</sub>H<sub>24</sub>N<sub>10</sub>O<sub>6</sub>S<sub>2</sub>Zn (**2**, *M* = 822.14): monoclinic, space group *P2<sub>1</sub>/n* (no. 13), *a* = 7.4144(6) Å, *b* = 10.0591(8) Å, *c* = 26.668(2) Å,  $\beta$  = 93.175(3)°, *V* = 1985.9(3) Å<sup>3</sup>, *Z* = 2, *T* = 150(2) K,  $\mu$ (MoK $\alpha$ ) = 0.780 mm<sup>-1</sup>, *D*<sub>calc</sub> = 1.375 g m<sup>-3</sup>, 95 334 reflections measured (5.62 ≤ 2 $\theta$  ≤ 65.74), 7409 unique (*R*<sub>int</sub> = 0.0441, *R*<sub>sigma</sub> = 0.0237), which were used in all calculations. The final *R*<sub>1</sub> was 0.0708 (*I* > 2 $\sigma$ (*I*)) and *wR*<sub>2</sub> was 0.1952 (all data).

Crystal data for C<sub>36</sub>H<sub>24</sub>I<sub>0.26</sub>N<sub>10</sub>O<sub>6</sub>S<sub>2</sub>Zn (**2·I<sub>2</sub>**, *M* = 855.14): monoclinic, space group *P2<sub>1</sub>m* (no. 10), *a* = 7.3967(13) Å, *b* = 10.0457(13) Å, *c* = 13.636(2) Å,  $\beta$  = 102.788(17)°, *V* = 988.1(3) Å<sup>3</sup>, *Z* = 1, *T* = 150(2) K,  $\mu$ (CuK $\alpha$ ) = 3.929 mm<sup>-1</sup>, *D*<sub>calc</sub> = 1.437 g m<sup>-3</sup>, 7437 reflections measured (12.28 ≤ 2 $\theta$  ≤ 153.06), 2169 unique (*R*<sub>int</sub> = 0.0407, *R*<sub>sigma</sub> = 0.0262), which were used in all calculations. The final *R*<sub>1</sub> was 0.1303 (*I* > 2 $\sigma$ (*I*)) and *wR*<sub>2</sub> was 0.4070 (all data).

## Electrochemistry

Cyclic voltammetry (CV) was performed using a BASi Epsilon Electrochemical Analyzer with ferrocene (Fc) as an internal reference. Measurements were conducted under an inert Ar atmosphere using a conventional three-electrode cell: a glassy carbon working electrode, a Pt wire auxiliary electrode, and a Ag/Ag<sup>+</sup> quasi-reference electrode. A [*n*Bu<sub>4</sub>N]PF<sub>6</sub>/MeCN electrolyte (0.1 M) was employed. Solution-state samples were measured with scan rates in the range 25–250 mV s<sup>-1</sup>. Solid-state samples were mounted on the glassy-carbon working electrode by dipping the electrode into a paste made of the powder sample in MeCN, and measured with scan rates in the range 100–1000 mV s<sup>-1</sup>.

## Solution state UV/Vis-NIR SEC

Spectroelectrochemistry over the range of 4000–35 000 cm<sup>-1</sup> was performed using a CARY 5000 spectrophotometer interfaced to Varian WinUV software. In the solution state, the absorption spectra of the electrogenerated species were obtained in situ by the use of an Optically Semi-Transparent Thin-Layer Electrochemical (OSTLE) cell, path length 0.65 mm, mounted in the path of the spectrophotometer. Solutions for the spectroelectrochemical experiment contained [*n*Bu<sub>4</sub>N]PF<sub>6</sub>/MeCN supporting electrolyte (0.1 M) and approximately 1 mM of the compound. Appropriate potentials were applied by using an eDAQ e-corder 410 potentiostat and the current was carefully monitored throughout the electrolysis. By this method, the electrogenerated species were ob-

tained in situ, and their absorption spectra were recorded at regular intervals throughout the electrolysis. The attainment of a steady-state spectrum and the decay of the current to a constant minimum at a potential appropriately beyond  $E_{1/2}$  (for the redox process in question) was indicative of the complete conversion of the starting material. The reversibility of the spectral data was confirmed by the observation of stable isosbestic points, and the regeneration of the starting spectrum.

### Solid-state Vis-NIR SEC

In the solid state, the diffuse reflectance spectra of the electrogenerated species were collected in situ in  $[n\text{Bu}_4\text{N}]\text{PF}_6/\text{MeCN}$  electrolyte (0.1 M) over the range 5000–22 500  $\text{cm}^{-1}$  using a Harrick Omni Diff Probe attachment and a custom built solid-state spectroelectrochemical cell described previously.<sup>[19]</sup> The cell consisted of a Pt wire counter electrode and  $\text{Ag}/\text{Ag}^+$  quasi-reference electrode. The solid sample was immobilized onto a 0.1 mm thick indium tin oxide (ITO)-coated quartz slide (which acted as the working electrode) using a thin strip of Teflon tape. The applied potential (from  $-2.5$  V to  $3.0$  V) was controlled using an eDAQ potentiostat. Continuous scans of the sample were taken and the potential varied gradually until change in the spectrum was observed.

### DFT calculations

Standard DFT calculations were carried out with Gaussian 09.<sup>[26]</sup> Geometries were obtained either in the gas phase or with the inclusion of a solvent continuum. For the gas-phase calculations, geometries were optimized at the B3-LYP/6–31G(d) level. For the condensed-phase optimizations, the SMD continuum solvation model<sup>[27]</sup> was used in conjunction with M05–2X/6–31G(d),<sup>[28]</sup> as recommended for use with the SMD model. The parameters for MeCN were employed in the SMD calculations to reflect the experimental conditions. For both the gas- and condensed-phase optimized structures, the vibrational frequencies of stationary points were inspected to ensure that they corresponded to minima on the potential energy surface. In all cases, we found that the two sets of optimized structures and the associated Kohn–Sham orbitals did not differ significantly.

### Powder X-ray diffraction (PXRD)

PXRD data were obtained using a PANalytical X'Pert PRO Multi-Purpose Diffractometer producing  $\text{Cu}_{\text{K}\alpha}$  ( $\lambda = 1.5406 \text{ \AA}$ ) radiation, equipped with a solid-state PIXcel detector. Samples were collected at a rate of  $0.028^\circ \text{ min}^{-1}$  over the interval  $5 \leq 2\theta \leq 50^\circ$  with a step size of  $0.013^\circ$ . Powder pattern simulations from SCXRD data were generated using the program Mercury 3.0.<sup>[29]</sup>

### EPR spectroscopy

A cw-EPR spectrum of  $1^-$  was obtained on a Bruker spectrometer (X-band, 9.337 GHz) with a sweep width of 500 G, modulation amplitude of 1 G, and microwave power of 3.95 mW. The data were averaged over 4 scans.

### Acknowledgements

We gratefully acknowledge support from the Australian Research Council and generous grants of computer time from the National Computational Infrastructure and Intersect Aus-

tralia Ltd. We also thank the ARC and Wellcome Trust for the provision of the EPR spectrometer.

**Keywords:** density functional calculations • donor–acceptor systems • electron transfer • metal–organic frameworks • spectroelectrochemistry

- [1] S. R. Batten, N. R. Champness, X.-M. Chen, J. Garcia-Martinez, S. Kitagawa, L. Ohrstrom, M. O'Keeffe, M. P. Suh, J. Reedijk, *Pure Appl. Chem.* **2013**, *85*, 1715.
- [2] C. J. Kepert, *Chem. Commun.* **2006**, 695.
- [3] a) T. Devic, C. Serre, in *Ordered Porous Solids: Recent Advances and Prospects* (Eds.: V. Valtchev, S. Mintova, M. Tsapatsis), Elsevier B. V., Amsterdam, **2009**, pp. 78–99; b) S. Kitagawa, R. Kitaura, S. Noro, *Angew. Chem.* **2004**, *116*, 2388; *Angew. Chem. Int. Ed.* **2004**, *43*, 2334.
- [4] a) D. M. D'Alessandro, J. R. R. Kanga, J. S. Caddy, *Aust. J. Chem.* **2013**, *64*, 718; b) G. Givaja, P. Amo-Ochoa, C. J. Gomez-Garcia, F. Zamora, *Chem. Soc. Rev.* **2012**, *41*, 115.
- [5] M. Kurmoo, *Chem. Soc. Rev.* **2009**, *38*, 1353.
- [6] Y. Sakata, S. Furukawa, M. Kondo, K. Hirai, N. Horike, Y. Takashima, H. Uehara, N. Louvain, M. Meilikhov, T. Tsuruoka, S. Isoda, W. Kosaka, O. Sakata, S. Kitagawa, *Science* **2013**, *339*, 193.
- [7] T. C. Narayan, T. Miyakai, S. Seki, M. Dincă, *J. Am. Chem. Soc.* **2012**, *134*, 12932.
- [8] a) S. Ando, J. I. Nishida, H. Tada, Y. Inoue, S. Tokito, Y. Yamashita, *J. Am. Chem. Soc.* **2005**, *127*, 5336; b) J. Y. Jung, M. Kang, J. Chun, J. Lee, J. Kim, J. Kim, Y. Kim, S. J. Kim, C. Lee, J. Yoon, *Chem. Commun.* **2013**, *49*, 176.
- [9] T. W. Lee, N. S. Kang, J. W. Yu, M. H. Hoang, K. H. Kim, J. I. Jin, D. H. Choi, *J. Polym. Sci. Part A* **2010**, *48*, 5921.
- [10] a) S. Van Mierloo, K. Vasseur, N. Van den Brande, A. E. Boyukbayram, B. Ruttens, S. D. Rodriguez, E. Botek, V. Liegeois, J. D'Haen, P. J. Adriaensens, P. Heremans, B. Champagne, G. Van Assche, L. Lutsen, D. J. Vanderzande, W. Maes, *ChemPlusChem* **2012**, *77*, 923; b) H. Z. Akpinar, Y. A. Udum, L. Toppare, *J. Polym. Sci. Part A* **2013**, *51*, 3901.
- [11] S. Van Mierloo, A. Hadipour, M. J. Spijkman, N. Van den Brande, B. Ruttens, J. Kesters, J. D'Haen, G. Van Assche, D. M. de Leeuw, T. Aernouts, J. Manca, L. Lutsen, D. J. Vanderzande, W. Maes, *Chem. Mater.* **2012**, *24*, 587.
- [12] I. Osaka, R. Zhang, J. Liu, D.-M. Smilgies, T. Kowalewski, R. D. McCullough, *Chem. Mater.* **2010**, *22*, 4191.
- [13] A. Heckmann, C. Lambert, *Angew. Chem.* **2012**, *124*, 334; *Angew. Chem. Int. Ed.* **2012**, *51*, 326.
- [14] a) F. E. Goodson, S. I. Hauck, J. F. Hartwig, *J. Am. Chem. Soc.* **1999**, *121*, 7527; b) H. Murata, D. Miyajima, H. Nishide, *Macromolecules* **2006**, *39*, 6331.
- [15] J. Cui, A. Wang, N. L. Edleman, J. Ni, P. Lee, N. R. Armstrong, T. J. Marks, *Adv. Mater.* **2001**, *13*, 1476.
- [16] Z. Ning, Z. Chen, Q. Zhang, Y. Yan, S. Qian, Y. Cao, H. Tian, *Adv. Funct. Mater.* **2007**, *17*, 3799.
- [17] N. G. Connelly, W. E. Geiger, *Chem. Rev.* **1996**, *96*, 877.
- [18] C. Lambert, W. Gaschler, E. Schmalzlin, K. Meerholz, C. Brauchle, *J. Chem. Soc. Perkin Trans. 2* **1999**, 577.
- [19] P. M. Usov, C. Fabian, D. M. D'Alessandro, *Chem. Commun.* **2012**, *48*, 3945.
- [20] P. J. Zapf, R. L. LaDuca, R. S. Rarig, K. M. Johnson, J. Zubieta, *Inorg. Chem.* **1998**, *37*, 3411.
- [21] a) S. Hisamatsu, H. Masu, I. Azumaya, M. Takahashi, K. Kishikawa, S. Kohmoto, *Cryst. Growth Des.* **2011**, *11*, 5387; b) J. R. Johnson, R. Ketcham, *J. Am. Chem. Soc.* **1960**, *82*, 2719.
- [22] CrysAlisPro, Yarnton, Oxfordshire. OX5 1QU, UK.
- [23] SAINT-Plus, Bruker AXS Inc., Madison, Wisconsin, **1995**.
- [24] L. Palatinus, G. Chapuis, *J. Appl. Crystallogr.* **2007**, *40*, 786.
- [25] G. M. Sheldrick, *SHELX97 programs for crystal structure analysis*, University of Göttingen. Institut für Anorganische Chemie der Universität, Tammanstrasse 4, 3400 Göttingen, Germany, **1998**.
- [26] Gaussian 09, Revision C.01, M. J. Frisch, G. W. Trucks, H. B. Schlegel, G. E. Scuseria, M. A. Robb, J. R. Cheeseman, G. Scalmani, V. Barone, B. Menucci, G. A. Petersson, H. Nakatsuji, M. Caricato, X. Li, H. P. Hratchian,

- A. F. Izmaylov, J. Bloino, G. Zheng, J. L. Sonnenberg, M. Hada, M. Ehara, K. Toyota, R. Fukuda, J. Hasegawa, M. Ishida, T. Nakajima, Y. Honda, O. Kitao, H. Nakai, T. Vreven, J. A. Montgomery, Jr., J. E. Peralta, F. Ogliaro, M. Bearpark, J. J. Heyd, E. Brothers, K. N. Kudin, V. N. Staroverov, R. Kobayashi, J. Normand, K. Raghavachari, A. Rendell, J. C. Burant, S. S. Iyengar, J. Tomasi, M. Cossi, N. Rega, J. M. Millam, M. Klene, J. E. Knox, J. B. Cross, V. Bakken, C. Adamo, J. Jaramillo, R. Gomperts, R. E. Stratmann, O. Yazyev, A. J. Austin, R. Cammi, C. Pomelli, J. W. Ochterski, R. L. Martin, K. Morokuma, V. G. Zakrzewski, G. A. Voth, P. Salvador, J. J. Dannenberg, S. Dapprich, A. D. Daniels, Ö. Farkas, J. B. Foresman, J. V. Ortiz, J. Cioslowski, D. J. Fox, Gaussian, Inc. Wallingford CT, **2009**.
- [27] A. V. Marenich, C. J. Cramer, D. G. Truhlar, *J. Phys. Chem. B* **2009**, *113*, 6378.
- [28] Y. Zhao, N. E. Schultz, D. G. Truhlar, *J. Chem. Theory Comput.* **2006**, *2*, 364.
- [29] C. F. Macrae, P. R. Edgington, P. McCabe, E. Pidcock, G. P. Shields, R. Taylor, M. Towler, J. van de Streek, *J. Appl. Crystallogr.* **2006**, *39*, 453.

---

Received: September 1, 2014

Published online on ■ ■ ■, 0000

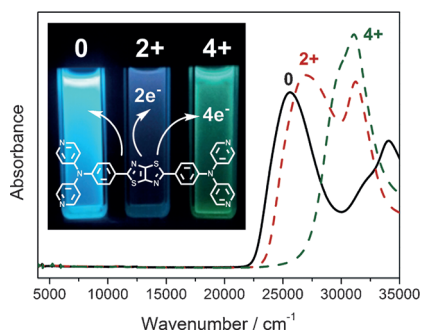
## FULL PAPER

### Electrochemistry

F. J. Rizzuto, T. B. Faust, B. Chan, C. Hua,  
D. M. D'Alessandro,\* C. J. Kepert\*



Experimental and Computational  
Studies of a Multi-Electron Donor–  
Acceptor Ligand Containing the  
Thiazolo[5,4-*d*]thiazole Core and its  
Incorporation into a Metal–Organic  
Framework



**Give and take:** A donor–acceptor–donor ligand, specifically designed to exhibit charge transfer, promotes conversion to diamagnetic cations during oxidation, each of which fluoresces at different wavelengths. Upon its incorporation into a metal–organic framework, the reducible nature of the thiazolo[5,4-*d*]thiazole core is carried forward, whereas oxidation processes cease altogether.